Flame Synthesis of Pd-TiO_2 Nanocomposite Catalyst for Oxygen Removal from CO_2-rich Streams in Oxy Combustion Exhaust

Sungyoon Jung[1,1], Nathan Reed[1], Gregory Yablonsky[1], and Pratim Biswas[1]

[1]Washington University in St. Louis

April 28, 2020

Abstract

Pd-TiO_2 catalysts with five Pd loadings were synthesized using a flame aerosol reactor. Their initial and changed catalytic properties and kinetic characteristics during/for O_2 removal with CH_4 were investigated. Different Pd loadings affected the size of Pd sub-nano clusters/nanoparticles and the speciation fraction of Pd (metallic Pd, PdO and PdO_x ($0 \langle x \langle 1$)). Increased size of Pd nanoparticles on catalysts' surface due to sintering and the reduction of PdO to metallic Pd or/and PdO_x were observed during the reaction. Fractions of the total surface area of Pd species were calculated, and correlations to the apparent reaction rate constants were established. Apparent kinetic constants were linearly proportional to fractions of total surface areas of metallic Pd or/and reduced Pd oxide were revealed, representing the intrinsic active site. The linear correlation between the O_2 reaction rate and the CO_2 concentration in the initial gas stream was also observed due to an autocatalytic reaction effect.

1. Introduction

The emission of CO_2 from fossil fuel combustion in power plants is one of the dominating contributors to global warming.[1,2] The U.S. Energy Information Administration reported that more than 60% of the energy in the U.S. was produced by fossil fuel combustion in 2018, and approximately half of it was generated from coal combustion.[3] Based on this percentage, energy-related CO_2 emission from coal combustion in 2018 was reported as approximately 1.3 Gt which was 24% of the total CO_2 emissions from fuel sources.[4] To mitigate the CO_2 level in the atmosphere, alternative energy sources, such as nuclear power and renewable energy, can be used,[1] but they currently cannot meet the immediate energy demand. Fossil fuel combustion is still necessary,[1] so removing CO_2 from fossil fuel combustion remains a pressing need.

Oxy combustion is a promising technique that has improved combustion efficiency and produces a flue gas with a high concentration of CO_2, which can be effectively captured.[1,2,5,6] Conventional coal combustion uses air, which dilutes the CO_2 concentration in the flue gas and thus requires an additional process (e.g., amine stripping) to capture CO_2 from the diluted flue gas. Oxy combustion uses highly pure O_2 (>95%) instead of air, which results in high combustion efficiency, low fuel consumption, and a concentrated CO_2 stream.[1,6] The captured CO_2 can be either sequestered[7] or reused for enhanced oil recovery (EOR).[8] Although a high concentration of CO_2 (˜63%) in the flue gas can be achieved, it cannot be directly applied for EOR or sequestration because the residual concentration of O_2 (˜3%) is higher than the requirement for EOR (<100 ppmv).[9] Therefore, O_2 must be removed from the flue gas before reuse.

Catalytic O_2 removal with hydrocarbons (e.g., methane) is one promising solution. Up until now, studies have focused on catalytic CH_4 combustion for generating energy in gas turbine combustors, and on using metal doped catalysts to decrease emissions.[10-13] There has been progress toward effective CH_4 oxidation at low temperature (<773 K) and considerable work in studies of this system at different compositions, temperatures, and pressures over different metal doped catalysts (e.g., Pd-Al_2O_3, Pt-Al_2O_3, Pd-SiO_2).[11,14] However, there is a significant difference between prior catalytic CH_4combustion studies and this work. Most

previous studies on catalytic CH_4 combustion used a relatively high O_2concentration with N_2 or He, as the balance of the gas, or relatively low concentrations of CO_2(<20%) to investigate their effects on the reaction. The challenge of this work is to decrease oxygen levels in low concentration O_2 streams (from 3% to less than 100 ppmv) in a highly concentrated CO_2 stream. Recent studies have shown the catalytic O_2 removal with CH_4 as a promising technique, and reported high O_2 conversions (>95%) by using noble metal doped catalysts (e.g., Pd-zeolite and Pd (or PdCu)-Al_2O_3).[15,16]Even though high O_2 conversion was achieved, two important aspects affecting the catalytic activity for O_2 removal were not fully investigated. First, active sites of the catalysts were not clearly elucidated. Noble metals such as Pd and Pt are known to have high catalytic activity for various applications.[11,17-22] However, there is still an ongoing debate on the active phase of noble metals for catalytic performance.[19-22] For example, the catalytic CH_4 combustion with noble metal supported catalysts strongly depends on the oxidation state of noble metal: Schmal et al.[19] reported that the coexistence of PdO and $PdO^{\delta+}$ played a crucial role in the enhanced CH_4 combustion. Yang et al.[23] showed that Pd^0/PdO_x (0<x[?]1) was the active phase for CH_4 combustion. To design a catalyst which has higher catalytic activity for O_2removal, it is necessary to fully understand the active phase of noble metal. Second, the effect of excess CO_2 in the initial gas stream on the catalytic performance for O_2 removal has not been explored. Therefore, additional efforts are required to develop effective O_2 removal from oxy combustion systems.

Metal oxide catalysts doped by noble metals have been extensively researched for oxidation studies.[11,24] To synthesize these catalysts, several methods, e.g., wet impregnation, sol-gel, and precipitation, have been widely utilized. However, these methods require additional processes, such as drying and calcination.[25] Unlike these methods, flame synthesis is a continuous one-step process that can be scaled up for high throughput production of nanoparticles.[26-28]Furthermore, many researchers have reported higher catalytic activity of flame-made catalysts due to their excellent dispersion of metal clusters on a metal oxide support.[29-31] Recently, Fujiwara et al.[32,33] synthesized sub-nano scale metal clusters on a metal oxide support by controlling the residence time in a flame and reported a much higher fraction of metal atoms on the catalyst surface and strong metal-support interaction, both of which enhanced the catalytic activity. In addition, Wang et al.[34]developed size-controlled Pt (<2 nm) doped TiO_2 films and found that the size of the Pt particles plays a crucial role in CO_2 photoreduction. However, there is still insufficient information about the fate of the nanoparticle catalysts and its correlation to the active phase of materials during the oxidation reaction.

In this study, Pd-TiO_2 catalysts were synthesized by using a flame aerosol reactor. The kinetic characteristics of the synthesized catalysts for O_2 removal were evaluated. Pd-TiO_2 catalysts were synthesized with five different Pd loadings to investigate their catalytic properties. Their changed catalytic properties during the reaction were also investigated. The total surface area of different Pd species (metallic Pd, PdO and PdO_x (0<x<1)) in the as-prepared and the treated catalysts was calculated for every loading, and the relationship between the fraction of the total surface area of different Pd species and apparent reaction rate constant was established. In kinetic experiments, the effect of different initial gas compositions on O_2 removal was investigated. The goal of this paper is to develop an efficient correlation between structural characteristics and steady-state kinetic characteristics that characterize the prepared catalysts. This relationship can be used as an important tool for primary kinetic characteristics of the catalyst and further catalyst design.

2. Experimental section

The synthesis method is described first, followed by characterization methods, and finally, a test plan is presented.

2.1 Synthesis of Pd-TiO_2 catalysts using a flame aerosol reactor (FLAR)

The experimental setup for synthesizing Pd-TiO_2catalysts is shown in Figure S1a in Supporting Information. The flame aerosol reactor (FLAR) system includes a precursor feeding system (bubbler and nebulizer), a diffusion burner, and a quenching and collection system. The bubbler was used for feeding titanium tetra-isopropoxide (TTIP, 99.7%, Sigma-Aldrich) with an N_2 carrier gas (1 L min^{-1}). The temperature of the oil bath in which the bubbler was placed was maintained at 323 K. The precursor delivery tubes were maintained

at around 373 K. The saturated TTIP precursor vapor was introduced into the central port of the burner. Palladium acetylacetonate ($Pd(acac)_2$, 97%, Sigma-Aldrich) was used as a dopant precursor, and it was dissolved in xylene (reagent grade, Sigma-Aldrich) and acetonitrile (99.8%, Sigma-Aldrich) mixture (2:1, v/v). In this study, five different Pd-TiO_2 catalysts were synthesized by controlling the concentration of the Pd precursor solutions (0.5 mM ˜3.0 mM). A three-jet Collison nebulizer was used to generate spray droplets, which were introduced to the central port of the burner. CH_4 and O_2 were introduced through the second and the outer port of the burner, respectively, with flow rates of 0.35 L min^{-1} and 2.5 L min^{-1}. The distance between the quench ring and the top of the burner was fixed at 3.8 cm. The synthesized catalysts were collected using an isopore membrane filter.

2.2 Characterization of synthesized Pd-TiO_2catalysts

The elemental analysis was conducted by both inductively coupled plasma mass spectroscopy (ICP-MS, Elan DRC ii, PerkinElmer) and field scanning electron microscopy (FESEM, JEOL 7001LVF FE-SEM, JEOL Ltd.) coupled with energy disperse X-ray spectroscopy (EDS). X-ray diffraction (XRD, Bruker d8 advance, Bruker) was utilized to investigate the crystallinity of the synthesized Pd-TiO_2 catalysts by using CuKα radiation (λ = 1.5418 Å) and a step size of 0.02°. The morphology and size of the synthesized catalysts were determined by scanning transmission electron microscopy (STEM) (TEM, JEOL 2100F, Jeol). The oxidation state of Pd was evaluated by X-ray photoelectron spectroscopy (XPS, Versa probe ii, Physical Electronics). Analyses for ICP-MS, XRD, and XPS were performed in triplicate. FESEM-EDS and STEM analyzed many spots for representative data. To investigate the changes in the catalytic properties, catalysts were treated at elevated temperatures up to 773 K for around 1 hr each temperature under the same experimental conditions and hereafter denoted as treated catalysts. They were further characterized by using the same analytical tools mentioned above.

2.3 Experimental setup and procedure

Figure S1b shows a differential fixed-bed reactor system. The feed gases are supplied from gas cylinders, and the gas composition is controlled by mass flow controllers. The differential fixed-bed reactor has three indentations in the middle to hold catalysts with glass fiber. Due to the low flowrate (˜ 3 mL min^{-1}), the glass fiber supports the catalyst well. A thermometer and temperature controller (Econo Temperature Controller, ACE Glass Inc.) are used for temperature control. To perform an experiment, 10 mg of the catalyst was loaded into the reactor. The experiment was conducted at temperatures ranging between 298 K and 773 K and under atmospheric pressure. The gas feed stream consisted of O_2 and CH_4 in balance CO_2, with a total flow rate of 3.2 mL min^{-1}. In this study, three different CO_2 concentrations (i.e., 0%, 53%, and 95% in balance He), and three different ratios between O_2 and CH_4 concentrations (i.e., O_2 rich composition: $O_2/CH_4 \cong 2.4$, stoichiometric composition: $O_2/CH_4 \cong 2.0$, O_2 lean composition: $O_2/CH_4 \cong 1.6$) were used. The compositions of the gas streams were sampled through an automatic gas valve and measured by gas chromatography (GC, 7890B, Agilent Technologies, Inc.), using helium as a carrier gas. The GC was equipped with a porous layer open tubular (PLOT) capillary column (Supelco Carboxen-1010) and a thermal conductivity detector (TCD).

3. Results and discussion

3.1 Flame synthesis of the catalysts and their structures' characterization

During the synthesis process, TTIP vapors generated from the bubbler and Pd precursor acetylacetonate salts decompose at the different temperature regions in the flame.[26] In the lower temperature region of the flame, TTIP vapors first form TiO_2 monomers, which subsequently undergo particle growth by collision, coalescence, and sintering. In the higher temperature region of the flame, Pd acetylacetonate salts decompose to form Pd vapor molecules, which can either condense or nucleate and subsequently be deposited on the surface of the created TiO_2 nanoparticles.[26] The condensed or deposited Pd molecules on the surface further diffuse and coalesce.[33] Varying the Pd concentrations can change the possibility of colliding with other molecules on the surface, which results in different sizes of Pd clusters/particles on the TiO_2 surface, and a previous study reported increasing sizes of Pd clusters on the TiO_2 surface with increasing Pd loading.[33]

Also, under the flame synthesis conditions, different Pd species (e.g., metallic Pd and PdO) can be expected. At high temperature, some oxidation of Pd can occur due to the presence of excess oxygen.[35] For the same residence time in the flame, the oxidation extent of metal might depend on the metal concentration. In this study, five different Pd-TiO_2 catalysts were synthesized by varying the concentration of Pd precursor solution from 0.5 mM to 3.0 mM. The synthesized Pd-TiO_2 catalysts were characterized by different analytical tools, as described below.

3.1.1 Determining Pd loadings (ICP-MS and FESEM-EDS)

ICP-MS confirmed the existence of Pd in the Pd-TiO_2catalysts, and the specific Pd loading was determined by the same instrument (Table 1). As can be seen in Table 1, the Pd loading values (wt%) obtained from ICP-MS increased from 0.24 wt% to 1.25 wt% with increasing concentrations of Pd precursor solution. It is worth noting that similar Pd loadings were obtained by FESEM-EDS, which reveals that most Pd particles were distributed on the catalyst surface, not in the bulk structure. It should be also noted that the treated catalysts at 773 K showed similar Pd loadings (data not shown), which implies that most Pd particles were still dispersed on the catalyst surface. The values obtained by ICP-MS were used for clarification of catalysts and further calculations. The five different Pd-TiO_2catalysts are hereafter denoted as catalyst 1 (0.24 wt% Pd), catalyst 2 (0.45 wt% Pd), catalyst 3 (0.76 wt% Pd), catalyst 4 (1.08 wt% Pd), and catalyst 5 (1.25 wt% Pd), respectively. Based on the ICP-MS analytical results, the total Pd masses in 10 mg of Pd-TiO_2 catalyst ($M_{\text{Total Pd}}$), the mass used for all experiments, were calculated$(10,000\ (\mu\gamma) \times \textit{Total Pd loading}\ (wt\%)/100)$and are shown in Table 1. As the concentrations of Pd precursor solution are increased, $M_{\text{Total Pd}}$ also increases, from 23.98 μg to 125.25 μg.

3.1.2 Distinguishing crystallinities of the catalysts and phase transformation (XRD)

The crystal structures of the synthesized fresh and the treated Pd-TiO_2 catalysts were evaluated by XRD, and Figure 1 shows their XRD spectra in the 2ϑ range of 20° to 60°. In the case of the fresh catalysts, a distinct peak of anatase (101) TiO_2 was obtained at a 2ϑ angle of 25.3°, and low-intensity of anatase (004), anatase (200), and anatase (211) peaks were observed at 2ϑ angles of 37.8°, 48.1°, and 55.1°, respectively. The XRD patterns revealed that the fresh catalysts have only TiO_2 anatase crystal structure, which correlates well with the JCPDS patterns of anatase (00-021-1272). In addition, the peak intensities for all crystal structures of Pd-TiO_2catalysts were very similar to each other and similar to that of the pristine TiO_2 catalyst, which indicates that the addition of Pd did not change the crystal structure of the TiO_2. On the other hand, distinct peaks for Pd metal and PdO were not observed, which might be due to the extremely low Pd loading or to the very small sizes of the Pd clusters/particles.

In the case of the treated catalysts, distinct peaks of anatase and rutile TiO_2 were obtained like the fresh catalysts: Noticeable peaks of anatase (101), anatase (004), anatase (200), and anatase (211) were observed. In addition to these anatase peaks, low-intensity of rutile (110) and rutile (101) peaks were obtained at a 2ϑ angle of 27.3° and 36.1°, respectively, which match with rutile phase of TiO_2 (JCPDS 75-1753). A slightly shifted peak of Ti_2O_3 (116) was also observed at approximately 54.2°. As can be seen in Figure 1b, all treated catalysts showed the peaks at the same 2ϑ angles, which indicates that they contain the mixed crystalline structures of TiO_2(anatase and rutile) and Ti_2O_3. However, the intensities of the observed peaks were somewhat different. To clearly see the differences, two magnified versions of figures are shown in Figure 1c (the pink-colored region at a 2ϑ angle ranging from 26° to 43° in Figure 1b) and Figure 1d (the grey-colored region at a 2ϑ angle ranging from 50° to 60° in Figure 1b). According to Figure 1c and 1d, it can be noted that the intensities of peaks of rutile (110), rutile (101), and Ti_2O_3 (116) were decreased as the Pd loading was increased from catalyst 1 to catalyst 5, while the peak intensity of anatase did not change much. Based on the obtained results, the intensity ratios between anatase (101) (I_{A101}, the strongest peak of anatase) and rutile (110) (I_{R110}, the strongest peak of rutile) and between I_{A101} and Ti_2O_3 (116) ($I_{Ti2O3116}$) were calculated. The calculated intensity ratio between I_{A101} and I_{R110} was decreased from 0.168 to 0.112 as the Pd loading was increased from catalyst 1 to catalyst 5. The calculated intensity ratio between I_{A101} and $I_{Ti2O3116}$ also showed the same decreasing trend from 0.184 to 0.166 with increasing the Pd loading. The previous study by Tiwari et al. [26] reported that the phase transformation of TiO_2 can be suppressed under

a high temperature condition by incorporating a noble metal dopant due to its surface modification. Our current result was consistent with this previous study. On the other hand, the low-intensity peak of PdO was observed with treated catalysts and its intensity was increased as the Pd loading was increased. This sudden appearance of PdO in treated catalysts can be attributed to the sintering effect of Pd on the TiO_2 surface, which will be discussed more in further sections.

3.1.3 Investigating similarities and differences of morphology and size of Pd and Pd-TiO_2 between fresh and treated catalysts (STEM)

The surface morphology and size of the synthesized fresh and treated Pd-TiO_2 catalysts were investigated by STEM (Figure 2). In each case, we counted more than 200 particles to evaluate the particle size distribution of the Pd-TiO_2 particles, and the results are shown in the first column of Figure 2a-e and in Table 1. In the case of the fresh catalyst, the five Pd-TiO_2catalysts had similar size distributions of their bulk structure, and similar average particle sizes ($d_{av,\ Pd-TiO_2}$): 7.57 ± 2.19 nm, 7.18 ± 2.07 nm, 7.61 ± 2.11 nm, 7.14 ± 1.04 nm, and 7.34 ± 1.91 nm, respectively (red-colored bars in the first column of Figure 2) (Table 1). The five fresh catalysts also had similar spherical shapes, as can be seen in the second column of Figure 2a-e. These results reveal that the addition of Pd did not change the particle morphology and size of the bulk structures. From STEM images, it was confirmed that there were no noticeable Pd subnano-clusters at the lowest Pd loading (catalyst 1) (Table 1). On the other hand, extremely small Pd subnano-clusters/nanoparticles (bright dots, circled in yellow in the second column of Figure 2), were observed. Pd subnano-clusters (<1 nm) were detected in catalysts 2 and 3, while both Pd subnano-clusters and Pd nanoparticles (>1 nm) were observed in catalysts 4 and 5 (Table 1). The size distributions of Pd subnano-clusters/nanoparticles in all cases were evaluated, and the results are shown with red-colored bars in the fourth column of Figure 2b-e and in Table 1. As can be seen in Figure 2 and Table 1, the average size of Pd subnano-clusters/nanoparticles ($d_{av,\ Pd}$) increased from 0.51 ± 0.12 nm to 1.04 ± 0.18 nm with increasing Pd loading (catalyst 2 to 5), which clearly demonstrates that Pd loading affects the size of Pd subnano-clusters/nanoparticles on the TiO_2 surface. Based on this trend, the size of Pd subnano-clusters in catalyst 1 can be assumed to be less than 0.5 nm.

In the case of the treated catalysts, the average particle sizes of Pd-TiO_2 were slightly increased to approximately 9 nm with the Pd loading was increased, as can be seen in the first column of Figure 2b-e (blue-colored bars). Based on this result, it can be noted that the sintering of the Pd-TiO_2 was not severe at the high temperature condition. Compared to the fresh catalysts showing very small Pd subnano-clusters and nanoparticles less than 1.5 nm, the treated catalysts showed larger nanoparticles and their average sizes were increased as the Pd loading was increased: 1.17 ± 0.26 nm for the treated catalyst 2, 1.41 ± 0.28 nm for the treated catalyst 3, and 2.27 ± 0.26 nm for the treated catalyst 4, respectively. Previous studies have reported the increased size of dopants on the support materials at the high temperature condition due to the sintering of them,[29,36] and our observation showed a similar trend. It is interesting to note that the treated catalyst 5 contains aggregates of Pd nanoparticles on the TiO_2 surface as well as the larger Pd nanoparticles. It has been known that the morphology of the nanoparticle can be affected by both the time for particle-particle collisions and the time for inter-particle coalescence (i.e. sintering).[37] When the time for particle-particle collisions is larger than the time for sintering, the particle coalesces before it collides with another particle, which results in the larger spherical particle. In the opposite case (the time for particle-particle collisions is smaller than the time for sintering), the particle collides with another particle before it coalesces, which causes the aggregates of the particles.[37] In this study, with the largest Pd loading (catalyst 5), the Pd nanoparticles could have more opportunity to collide with other Pd nanoparticles on the TiO_2surface. Thereby, the time for colliding can be smaller than the time for sintering, resulting in the aggregates of Pd nanoparticles on the TiO_2 surface as can be seen in the third column of Figure 2e. It is also worth noting that the morphology of the TiO_2 was changed to the porous structure, which might be due to the creation of the aggregates of Pd nanoparticles on it.

3.1.4 Distinguishing oxidation states of components in fresh and treated catalysts (XPS)

To investigate the effect of different Pd loadings on the Pd species in the synthesized Pd-TiO_2 catalysts, the Pd oxidation state in the fresh catalysts was evaluated by XPS, with the results shown in the left column

of Figure 3 and summarized in Table 2. Three Pd species were identified based on different characteristic Pd $3d_{5/2}$ core level binding energies: metallic Pd (335.7 eV), intermediate PdO_x (0<x<1) (336.42 eV), and PdO (337.4 eV).[29] As can be seen in Figure 3 and Table 2, the XPS spectra confirm that all the Pd-TiO_2 catalysts contained three Pd species, but the percentages of the three Pd species changed as the Pd loading changed. The amount of metallic Pd increased from 33.34 ± 1.23% to 42.32 ± 4.01% as Pd loading was increased from 0.24 wt% to 0.76 wt% (catalyst 1 to catalyst 3). The amount of metallic Pd decreased to 35.78 ± 2.89% as Pd loading was further increased to 1.25 wt% (catalyst 5). On the other hand, the amounts of intermediate PdO_x and PdO showed opposite trends to that of metallic Pd. As mentioned earlier in 3.1., the extent of the oxidation of Pd could be varied with different Pd loadings at the same flame-synthesizing condition. The results with the fresh catalysts here are in line with this hypothesis. To study the change in the Pd species at the high temperature under the same experimental condition, the Pd oxidation state in the treated catalysts was also characterized by XPS, and the results are shown in the right column of Figure 3 and Table S1. As shown in Figure 3, the treated catalysts also contained three Pd species, i.e. metallic Pd, PdO and PdO_x. Compared to the fresh catalysts, the proportions of metallic Pd and PdO_x were increased, while the percentage of PdO was decreased as the Pd loading was increased (Table S1). Previous studies revealed that the Pd^{2+} was reduced into Pd^0 and/or Pd^+ at the high temperature during methane oxidation reaction.[23,29] Our analytical results were consistent with these previous findings.

Furthermore, the changes in other species, Ti and O, were evaluated by XPS for both the fresh and the treated catalysts, and the results are shown in Figure S2, S3, Table S2, and Table S3. The Ti 2p spectra in both fresh and treated catalysts were deconvoluted into four peaks at approximately 456.7 eV, 458.5 eV, 460.3 eV, and 464.2 eV, which are denoted as $Ti^{3+}(2p_{3/2})$, Ti^{4+} $(2p_{3/2})$, Ti^{3+} $(2p_{1/2})$, and Ti^{4+} $(2p_{1/2})$.[38,39]This observation implies that Ti in both fresh and treated catalysts was mainly in TiO_2 phase, and the small amount of Ti was in Ti_2O_3 (Ti^{3+}) phase. Compared to the fresh catalysts, an increasing amount of Ti^{3+} was obtained. In addition, the percentage of Ti^{3+} was slightly decreased as the Pd loading was increased. These findings demonstrated the slight phase transformation of TiO_2 toward Ti_2O_3 and the suppressing effect of Pd on the phase transformation, which were matched with the XRD results in 3.1.2. It should be noted that the intensity of Ti was not different much among samples. For comparison, the XPS spectra of O is in both fresh and treated catalysts are shown in Figure S3 and Table S3. The XPS spectra of both fresh and treated catalysts showed three noticeable peaks, at approximately 529.9 eV, 531.3 eV, and 532.2 eV, which can be assigned respectively to (1) lattice oxygens in a fully-coordinated environment with metal ions (O_{lattice}), (2) oxygen deficient regions of the metal oxide ($O_{\text{deficient region}}$), and (3) adsorbed oxygen species, such as O_2, H_2O, or M(metal)-OH on the surface,[40] which might be produced during the catalyst synthesis process. We can term these species intrinsically adsorbed oxygen, or O_{adsorbed}. As can be seen Figure S3, there was no significant change in O_{lattice} in the fresh and treated catalysts. On the other hand, an increasing amount of $O_{\text{deficient region}}$ and a decreasing amount of O_{adsorbed}, which indicates the desorption of the adsorbed oxygen species at high temperature and the reduction of Ti and/or Pd.

In the previous sections and this section, it was confirmed that (1) most Pd was deposited on the TiO_2 surface, (2) size of Pd-TiO_2 was not changed much, and (3) the intensity of Ti was not different much among fresh and treated catalysts. Based on these results, the dispersion or sintering of Pd on the TiO_2 surface can be determined by comparing the ratio between the intensity of Pd 3d (I(Pd)) and Ti 2p (I(Ti)) in fresh and treated catalysts. The ratios were calculated, and they were compared by obtaining $(\frac{Treated(\frac{I(\text{Pd})}{I(\text{Ti})})}{Fresh(\frac{I(\text{Pd})}{I(\text{Ti})})})$ (Table S1). The calculated values were decreased as the Pd loading was increased, which could imply the decreased Pd coverage on the TiO_2 surface due to sintering of Pd. This is consistent with our STEM and XRD results showing the increasing size of Pd.

3.1.5 Total surface area of different Pd species

Based on the $M_{\text{Total Pd}}$ (Table 1) and XPS analytical results, the masses of metallic Pd ($M_{\text{metallic Pd}}$), PdO (M_{PdO}) and intermediate PdO_x(M_{PdO_x}) were calculated by

$$M_{\text{metallic Pd}}\ (\mu\gamma) = M_{\text{Total Pd}} \times \frac{Metallic\ Pd\ (\%)}{100}, \quad (1)$$

$$M_{\text{PdO}}\ (\mu\gamma) = M_{\text{Total Pd}} \times \frac{PdO\ (\%)}{100} \times \frac{\text{MW}_{\text{PdO}}}{\text{MW}_{\text{Pd}}}, \quad (2)$$

$$M_{\text{PdO}_x}\ (\mu\gamma) = M_{\text{Total Pd}} \times \frac{\text{PdO}_x\ (\%)}{100} \times \frac{\text{MW}_{\text{PdO}_x}}{\text{MW}_{\text{Pd}}}, \quad (3)$$

where MW_{Pd}, MW_{PdO} andMW_{PdO_x} represent the molar weights of Pd, PdO and PdO_x, respectively. It should be noted that most Pd subnano-clusters/nanoparticles were distributed on the catalyst's surface, which was demonstrated by ICP-MS and FESEM-EDS. Therefore, XPS analytical results could be combined here to calculate the masses of different Pd phases. MW_{PdO_x} was assumed to be an average of MW_{Pd} and MW_{PdO}. The calculated values based on the fresh catalysts are summarized in Table 2, where it can be seen that the mass of each Pd species does not depend on the fraction of Pd species, but instead depends on the Pd loading.$M_{\text{metallic Pd}}$, M_{PdO} andM_{PdO_x} increased from 8.00 μg, 9.06 μg and 8.72 μg, to 44.81 μg, 36.39 μg and 52.46 μg with increasing Pd loading (catalyst 1 to 5). The total surface area (TSA) of each Pd species was further calculated based on

$$\text{M}\ (\mu\gamma) = N \times \tfrac{\pi}{6} \times d^3 \times \rho, \quad (4)$$

$$\text{TSA}\ \left(\text{cm}^2\right) = \tfrac{6M}{\rho\delta} = N \times \pi \times d^2, \quad (5)$$

where N , d , and ρ represent the number, diameter, and density of each Pd species, respectively. For the calculation, the Pd species were assumed to have the same size and spherical shape of Pd subnano-clusters/nanoparticles, and an average density of metallic Pd and PdO was used for the density of PdO_x. Because of different masses and densities of the three different Pd species, different volumes and areas of them were expected. The calculated values are summarized in Table 2. It is worth noting that the TSAvalues of metallic Pd, PdO and PdO_x show different trends. $\text{TSA}_{\text{metallic Pd}}$ increases with increasing Pd loading (catalyst 2 to 3) and reaches the largest value of 245.56 cm^2. Then, it decreases as the Pd loading is further increased (catalyst 3 to 5). In the case of TSA_{PdO}, a similar trend is found, but the peak value of 296.35 cm^2 is found with catalyst 4. The$\text{TSA}_{\text{PdO}_x}$ increases with increasing Pd loading (catalyst 2 to 5) and reaches its largest value of 299.68 cm^2 with the highest Pd loading (catalyst 5). However, for any Pd phase (metallic Pd, PdO and PdO_x), the sample-by-sample TSA dependence exhibits the same trend as the percentage of this phase. In the case of the treated catalysts, the comparison was done among catalysts 2, 3 and 4, and the results are shown in Table S1. According to STEM analytical results, there were aggregates of Pd nanoparticles in the treated catalyst 5, and thereby the calculation based on the spherical shape of primary Pd particles could not be applied. As can be seen Table S1,$\text{TSA}_{\text{metallic Pd}}$ of the treated catalysts followed a similar trend to $\text{TSA}_{\text{metallic Pd}}$ of the fresh catalysts: $\text{TSA}_{\text{metallic Pd}}$ was increased from 85.68 cm^2 to 124.70 cm^2 as the Pd loading was increased (catalyst 2 to 3), and then it was decreased to 105.61 cm^2 as the Pd loading was further increased (catalyst 3 to 4). On the other hand, unlike the fresh catalysts,TSA_{PdO} and $\text{TSA}_{\text{PdO}_x}$ of the treated catalysts show a similar trend to$\text{TSA}_{\text{metallic Pd}}$ of the treated catalysts: Both were increased to 70.78 cm^2 and 131.74 cm^2 as the Pd loading was increased from catalyst 2 to catalyst 3, and further decreased to 64.75 cm^2 and 120.12 cm^2 as the Pd loading was increased to catalyst 4. It should be noted that all *TSA* of the treated catalysts were smaller than those of the fresh catalysts because Pd subnano-clusters/nanoparticles were sintered on the TiO_2surfaces at the high temperature. The TSA of metal could play a crucial role in the catalytic activity by providing active sites for the reaction, and thus higher catalytic activity is expected with the larger TSA of metal. Because the TSA of all Pd species showed different trends, the important Pd species on the catalytic activity in O_2 removal could be demonstrated, which is discussed in the following section.

3.2. Catalytic activity of the synthesized Pd-TiO_2 catalysts in O_2 removal

3.2.1 Catalytic activity evaluation in O_2 removal

The synthesized Pd-TiO_2 catalysts were evaluated for O_2 removal. The experiments were conducted under initial O_2 rich composition ($O_2/CH_4 \cong 2.4$), with excessive CO_2 as the balance of the gas. The experiments under other initial conditions are shown in the following section, 3.2.3. The O_2 and CH_4 conversions were calculated based on:

$$\text{Conversion } (\%) = \frac{C_i - C_f}{C_i} \times 100, \quad (6)$$

where C_i and C_f represent the initial and final concentrations of gas, respectively. Data on "conversion-temperature" dependencies are presented in Figure 4 and Table 3.

Our system consisted of six gaseous substances (CH_4, O_2, CO, H_2O, H_2 and CO_2) of three elements (C, H, O). Generally, three independent overall reactions are possible (6 substances – 3 elements = 3 independent overall reactions):

$$\text{(Complete } CH_4 \text{ oxidation) } CH_4 + 2O_2 \rightarrow CO_2 + 2H_2O, \quad H_{298} = -880\ kJ/mol, \quad (7)$$

$$\text{(Partial } CH_4 \text{ oxidation) } CH_4 + 1/2O_2 \rightarrow CO + 2H_2, \quad H_{298} = -35.6\ kJ/mol, \quad (8)$$

$$\text{(Dry reforming of } CH_4) \quad CH_4 + CO_2 \rightarrow 2CO + 2H_2, \quad H_{298} = 247.3\ kJ/mol. \quad (9)$$

All reactants and products were analyzed by using a GC. As can be seen in Figure 4a,b and Table 3, the concentrations of both O_2 and CH_4 decreased as the temperature was increased. CO_2 gas was detected, but in our typical experiment the CO_2 concentration was comparatively high, and its change was hard to monitor. On the other hand, there was no CO observed. In addition, the dry reforming reaction is highly endothermic and requires considerable external energy. The low temperature ([?]773 K) applied to our experimental system may not favor this reaction. Therefore, the partial CH_4 oxidation (Eq. 8) and dry reforming of CH_4 (Eq. 9) reactions can be ruled out. It is worth noting that there is no H_2 observed and thereby, water-gas shift reaction ($CO + H_2O \rightarrow CO_2 + H_2$) in the system is negligible.

To confirm the generation of CO_2 as a product via reaction (7), a separate experiment was performed with He gas as the balance of the gas instead of CO_2, with the results shown in Figure S4. Decreasing trends were found in the O_2 and CH_4 concentrations. Only CO_2 (no CO) was clearly observed as a product, and the total concentration of C remained constant during the reaction. Furthermore, the reaction rate of CH_4 is half the reaction rate of O_2 via reaction (7) ($R_{CH_4} = \frac{1}{2}R_{O_2}$). The reaction rate of both CH_4 and O_2 at 723 K and 773 K were summarized in Table S4. Table S4 indicates stoichiometry: the reaction rates of CH_4 are close to the half of reaction rates of O_2 at both 723 K and 773 K ($\left|\frac{R_{CH_4} - 1/2R_{O_2}}{R_{CH_4}}\right| \times 100 \leq 6$ %). Therefore, complete CH_4 oxidation (Eq. 7) was the single overall reaction in this system. All catalysts showed the same trends of reactant and product concentrations.

Figure 4 and Table 3 show an enhanced O_2 and CH_4 conversions with Pd-TiO_2 catalysts compared to those with only TiO_2(˜30.9% for O_2, and ˜50.7% for CH_4 at 723 K). This result emphasizes the importance of Pd in effective O_2 removal. In addition, O_2 conversion increased from 55.8% to 77.0% at 723 K with increasing Pd loading (catalyst 1 to 3). However, it decreased when the Pd loading was further increased (catalyst 3 to 5). CH_4 conversion was enhanced from 64.4% to 92.4% as Pd loading was increased (catalyst 1 to 3), and then no significant difference was observed as Pd loading was further increased.

3.2.2 Apparent reaction rate constant and total surface area of Pd species

Our preliminary experiments at different temperatures proved that the O_2 removal reaction with Pd-TiO_2catalysts followed an apparent first order reaction (Figure S5): the natural log of C_f/C_i plotted versus residence time (min) demonstrates a linear trend (R^2>0.92) at different temperatures. Therefore, the apparent reaction rate constant (k_{app}) can be determined by

$$\frac{\delta^{n}}{\delta\tau} = -k_{\mathrm{app}}C, \quad (10)$$

where C and τ represent the concentration of O_2 and residence time (min). The calculatedk_{app} values at 723 K are summarized in Table 3. It should be noted that when the plot of k_{app} and the total Pd loading was expressed (Figure 5a), an optimal total Pd loading was observed. Because different Pd species (metallic Pd, PdO and PdO_x) could be involved in the O_2removal reaction, the relationship between k_{app} and total Pd loading might not be sufficient to understand the active phase of Pd for the reaction. To reveal the active phase of Pd which is responsible for the catalytic activity, it is necessary to distinguish the contributions of different Pd species on the O_2 removal reaction. Also, it must be understood the change in the catalytic properties during the reaction and corresponding catalytic activity. In the interpretation of kinetic data, the hypothesis of additivity can be formulated. In accordance with this hypothesis, the reaction occurs on different Pd phases (i.e., metallic Pd, PdO and PdO_x). Previously, Kannisto et al. and Murzin[41,42] analyzed contributions of different geometric sites into the whole catalytic activity. Similar to their additive approach, k_{app} can be presented as a sum of different contributions:

$$k_{\mathrm{app}} = k_{app,metallid\ Pd}\alpha + k_{app,\ PdO}\beta + k_{app,\mathrm{PdO}_x}\gamma, \quad (11)$$

$$\alpha = \frac{\mathrm{TSA}_{\mathrm{metallic\ Pd}}}{\mathrm{TSA}_{\mathrm{total}}},\ \beta = \frac{\mathrm{TSA}_{\mathrm{PdO}}}{\mathrm{TSA}_{\mathrm{total}}},\ \gamma = \frac{\mathrm{TSA}_{\mathrm{PdO}_x}}{\mathrm{TSA}_{\mathrm{total}}}, \quad (12)$$

$$\alpha + \beta + \gamma = 1, \quad (13)$$

where $k_{app,\ metallic\ Pd}$, $k_{app,PdO}$ and$k_{app,\ \mathrm{PdO}_x}$ represent the apparent reaction rate constants on metallic Pd, PdO and PdO_x, respectively. The obtained k_{app} is presented as a function of fractions of the total surface area of each Pd species (α, $\beta$and γ). In this study, three different types of α, β and γ were obtained based on the analytical results of (1) fresh and (2) treated catalysts, and (3) averages of them: α_{fresh}, β_{fresh} andγ_{fresh} represent the fraction of the total surface area of metallic Pd, PdO and PdO_x, respectively, and those in the treated catalysts were denoted as$\alpha_{\mathrm{treated}}$, β_{treated} and$\gamma_{\mathrm{treated}}$, respectively. In addition,α_{avg}, β_{avg} andγ_{avg} were obtained by averaging the analytical results of fresh and treated catalysts. The relationships between the calculated k_{app} and α, β and γwere further investigated: The plots of k_{app} and fractions in the fresh catalysts (α_{fresh},β_{fresh} and γ_{fresh}) were expressed with temperatures near at which the catalytic activity was initiated. The plots of k_{app} and fractions in the treated catalysts ($\alpha_{\mathrm{treated}}$, β_{treated} and$\gamma_{\mathrm{treated}}$) were displayed with the high temperatures. The moderate temperatures were used for the plots of $k_{\mathrm{app}}$and average fractions (α_{avg}, $\beta_{\mathrm{avg}}$and γ_{avg}) as well. In the case of the fresh catalysts, a linear increase was observed with k_{app} andα_{fresh} (metallic Pd) (R^2>0.91) (Figure 5b), while as for the dependencies between k_{app} and β_{fresh}(PdO) and between k_{app} and γ_{fresh}(PdO_x), no correlation was found (Figure S6a,b). Therefore, it can be concluded that for the fresh catalysts, the apparent catalytic activity is governed by metallic Pd and the contribution of Pd oxides is insignificant.

In the cases of the treated catalysts and the averaged values, like the plot of k_{app} and α_{fresh} (metallic Pd),k_{app} was generally linearly increased as both$\alpha_{\mathrm{treated}}$ and α_{avg} were increased with R^2>0.85 and R^2>0.90, respectively (Figure 5c,d). No correlations between k_{app} and $\gamma_{\mathrm{treated}}$($PdO_x$) and between k_{app} andγ_{avg} were observed (Figure S7a,b). It is interesting to note that unlike the plot of k_{app} andβ_{fresh} (PdO), k_{app} was linearly decreased as both β_{treated} and β_{avg}were increased (Figure S8a,b). These results could indicate the metallic Pd is the active catalytic phase. However, it is risky to conclude that only metallic Pd plays a crucial role in the reaction. The catalysts generally go through a complex process during the reaction in which Pd oxides are partially reduced to metallic Pd or/and PdO_x (0<x<1) species, experimentally distinguished (see previous section 3.1.4). The calculatedk_{app} exhibited the linear dependence regarding the combined fractions of the total surface area of metallic Pd and PdO_x($\alpha_{\mathrm{treated}} + \gamma_{\mathrm{treated}}$) (Figure S9). The previous study by Yang et al.[23] reported the reduced form of Pd (Pd^0 and PdO_x(0<x<1)) was preferential for the effective methane oxidation reaction. A theoretical study by using density functional theory (DFT) calculations also revealed the lower activation energy barrier for methane decomposition, which is widely accepted as the reaction rate limiting step, on the reduced PdO surface.[43]Therefore, it could be concluded that metallic

Pd mainly controls the O_2 removal reaction and the reduced Pd phase, metallic Pd or/and PdO_x, at high temperature also generates an active phase for the reaction. Our interpretation of results of physico-chemical analysis and kinetic studies, showing the volcano-shaped dependencies (Figure 5a), emphasizes that the Pd loading itself does not affect the intrinsic catalytic property of the synthesized catalyst, but the fraction of active Pd phases, which are metallic Pd or/and reduced Pd (PdO_x), significantly determines it. Behind the volcano-shaped dependencies, a linear dependency between the k_{app} and the fraction of the total surface area of active Pd phases (metallic Pd or/and reduced form of Pd) results in the constant catalytic activity per unit area of metallic Pd or/and reduced form of Pd. It means that we observe the case of so-called structure insensitive catalytic system defined by Boudart.[44] For such systems, the catalytic activity per unit of area is related to the specific active component and does not dependent on the preparation method providing a guidance for the catalyst design.[44-46]

3.2.3 Influence of reactants and products: Autocatalytic effect; other reactions

The previous experiments were conducted under O_2 rich composition ($O_2/CH_4 \cong 2.4$). In this section, two different initial compositions were considered: first, different CO_2 concentrations (0% and 53%, He as the balance of the gas) under O_2 rich composition in the initial gas stream were applied. Second, different ratios between O_2 and CH_4 concentrations (i.e., stoichiometric composition: $O_2/CH_4 \cong 2.0$ and O_2 lean composition: $O_2/CH_4 \cong 1.6$ with excessive CO_2 as the balance of the gas) were tested.

To investigate the effect of CO_2 concentration in the initial gas stream on the O_2 removal (first initial composition), experiments with different CO_2concentrations (i.e., 0% and 53%, He as the balance of the gas) under O_2 rich composition were conducted, and their results and the previous result with 95% of CO_2 are shown in Figure 6. Complete CH_4 oxidation (Eq. 7) was the main reaction between CH_4 and O_2, which was proved by the closed values between the reaction rates of CH_4 and the half of reaction rates of O_2(Table S5). On the other hand, it should be noted that both O_2 and CH_4 conversions were enhanced as the CO_2 concentration was increased. To clearly see the correlation between the reaction rate and the initial CO_2 concentration, the O_2 reaction rate versus the initial CO_2 concentration was plotted in Figure S10. As can be seen in Figure S10, the O_2reaction rate was proportional to the initial CO_2concentration: the O_2 conversion rate ($mmol/g_{cat}/hr$) versus the concentration of initial CO_2 (mol/m^3) at different temperatures could be approximately explained by a linear dependence (R^2>0.88). It can be defined as an autocatalytic effect. In accordance with our knowledge, this effect can be shown by the linear correlation between the reaction rate and the concentration of product.[47] Previously, the autocatalytic effect on different applications has been reported and the accelerated reaction rates were mostly supported by the lower activation barriers via new intermediates.[48,49] Therefore, it could be concluded that CO_2 is itself involved in the O_2 removal reaction. The process may occur via CO_2-containing intermediates and the reaction rate is enhanced as the autocatalytic reaction. It is possible that the application of DFT calculations will be useful for understanding this effect.

Results under second initial composition were compared with the previous one which was performed under O_2 rich composition with excessive CO_2 as the balance of the gas (95%) in Figure 7. Figure 7 demonstrates: as the ratio between O_2 and CH_4 was decreased from the O_2 rich composition to the O_2 lean one, the conversion of O_2 was increased. For example, the O_2conversion was increased from 77% to 88% at 723 K, while the CH_4 conversion was decreased from 92% to 69%. This result indicates that more reaction source (CH_4) can enhance the O_2 conversion. It should be also noted that there was a sharp increase in the CH_4 conversion at around 723 K under O_2 lean condition (Figure 7b). This sudden increase in the CH_4 conversion could be due to the dry reforming of CH_4 reaction (Eq. 9). It can be supported by Figure 8, which shows: at high temperature (> 723 K), CO generates under only O_2 lean composition. It can be also shown by the reaction rates of CH_4, O_2, and CO which were summarized in Table S6. Via both complete CH_4 oxidation reaction (Eq. 7) and dry reforming of CH_4 reaction (Eq. 9), the reaction rate of CH_4 is the same as the difference between the half of the reaction rate of O_2 and the half of the reaction rate of CO. Table S6 demonstrates that there was both complete CH_4 oxidation reaction and dry reforming of CH_4 under O_2 lean composition at 773 K. A previous study reported the same trend which shows the decreasing CO_2 selectivity

due to the formation of CO under O_2 lean composition $O_2/CH_4 \cong 1.5$ and 1.75).[16] This experimental result implies that the excessive CH_4 could cause a nonpreferred reaction by reacting with CO_2 to generate CO.

4. Conclusions

Pd-TiO_2catalysts with varying Pd loading (0.24 wt% - 1.25 wt%) were synthesized by using a flame aerosol reactor, and the material and kinetic characteristics of the fresh catalysts and the treated catalysts at high temperature under the same experimental conditions were evaluated. Our study contributes to three major findings:

(1) In the case of the fresh catalysts, the addition of Pd did not change the crystal structure of the base TiO_2, and the size of the Pd-TiO_2 particle did not change with different Pd loadings, but the size of Pd subnano-clusters/nanoparticles and the oxidation state of Pd (metallic Pd, PdO and PdO_x) was significantly affected by Pd loading. In the case of the treated catalysts, small change in the phase of TiO_2 from anatase TiO_2 to both rutile TiO_2 and Ti_2O_3 was observed, but the phase transformation was suppressed with increasing of the Pd loading. Two major changes in Pd on the catalyst's surface were observed: First, increased size of Pd nanoparticles on the catalyst's surface was observed due to the sintering effect. With the highest Pd loading, aggregates of Pd nanoparticles on the catalyst's surface were obtained. Second, some amount of PdO was reduced to either metallic Pd or intermediate PdO_x.

(2) The total surface areas of different Pd species in the fresh and treated catalysts were evaluated based on the size distribution of Pd and fractions of Pd species. For the fresh catalysts, the apparent reaction rate constants were proportional to the calculated fraction of the total surface area (TSA) of metallic Pd. For the treated catalysts, a linear correlation between the apparent reaction rate constants and the combined fraction of TSA (metallic Pd and reduced Pd oxide, i.e. PdO_x ($0<x<1$)) was obtained as well. Different catalytic characteristics on Pd loading, i.e. the total surface area of metallic Pd, conversion of O_2 and apparent reaction rate constants, exhibit the volcano-shaped dependencies. However, behind these dependencies, a linear proportionality between apparent kinetic constants and fractions of total surface areas of metallic Pd or/and reduced Pd oxide is revealed using distinguishing different Pd phases, which represents the intrinsic activity of the active site.

(3) Two different initial conditions (i.e., different ratios between O_2 and CH_4 concentrations and different CO_2 concentrations) were tested and revealed CO generation at high temperature under O_2 lean condition. In addition, the reaction rate of O_2 had a linear dependency on the initial CO_2 concentration, which was indicated by an autocatalytic reaction effect.

This study provides structural and kinetic investigation on O_2 removal with flame-synthesized Pd-TiO_2 catalysts and emphasizes the kinetic role of metallic Pd and reduced Pd oxide, i.e. PdO_x($0<x<1$). This study also proposed a positive effect of initial CO_2 concentration on O_2removal via an autocatalytic reaction effect. Detailed role of dry reforming reaction under different initial conditions and autocatalytic reaction effect on O_2 removal will be addressed in our further study.

Acknowledgements

This work was supported by a grant funded by the U.S. Department of Energy's National Energy Technology Laboratory under Award Number DE-FE0029161.

References

1. Buhre BJP, Elliott LK, Sheng CD, Gupta RP, Wall TF. Oxy-fuel combustion technology for coal-fired power generation. *Prog. Energ Combust. Sci.* 2005;31(4):283-307.

2. Jordal K, Anheden M, Yan J, Strömberg L. Oxyfuel combustion for coal-fired power generation with CO_2capture-opportunities and challenges. *Greenhouse Gas Control Technologies.* 2005;7:201-209.

3. U.S. Energy Information Administration. What is U.S. electricity generation by energy source? 2018; https://www.eia.gov/tools/faqs/faq.php?id=427&t=3.

4. U.S. Energy Information Administration. U.S. Energy-related carbon dioxide emissions, 2018. 2019; https://www.eia.gov/environment/emissions/carbon/.

5. Gopan A, Kumfer BM, Phillips J, Thimsen D, Smith R, Axelbaum RL. Process design and performance analysis of a Staged, Pressurized Oxy-Combustion (SPOC) power plant for carbon capture. *Appl. Energ.* 2014;125:179-188.

6. Kanniche M, Gros-Bonnivard R, Jaud P, Valle-Marcos J, Amann JM, Bouallou C. Pre-combustion, post-combustion and oxy-combustion in thermal power plant for CO_2 capture. *Appl. Therm. Eng.* 2010;30(1):53-62.

7. Chu S. Carbon capture and sequestration. *Science*2009;325(5948):1599-1599.

8. Dai Z, Middleton R, Viswanathan H, Fessenden-Rahn J, Bauman J, Pawar R, Lee SY, McPherson B. An integrated framework for optimizing CO_2 Sequestration and enhanced oil recovery.*Environ. Sci. Technol. Lett* 2014;1(1):49-54.

9. DOE/NETL. Quality guidelines for energy system studies: CO_2 impurity design parameters. 2013.

10. Enger BC, Lødeng R, Holmen A. A review of catalytic partial oxidation of methane to synthesis gas with emphasis on reaction mechanisms over transition metal catalysts. *Appl. Catal. A*2008;346(1-2):1-27.

11. Gélin P, Primet M. Complete oxidation of methane at low temperature over noble metal based catalysts: a review. *Appl. Catal. B*2002;39(1):1-37.

12. Hoflund GB, Li Z, Epling WS, Göbel T, Schneider P, Hahn H. Catalytic methane oxidation over Pd supported on nanocrystalline and polycrystalline TiO_2, Mn_3O_4, CeO_2 and ZrO_2. *React. Kinet. Catal. Lett*2000;70(1):97-103.

13. Osman AI, Abu-Dahrieh JK, Laffir F, Curtin T, Thompson JM, Rooney DW. A bimetallic catalyst on a dual component support for low temperature total methane oxidation. *Appl. Catal. B*2016;187:408-418.

14. Muto K, Katada N, Niwa M. Complete oxidation of methane on supported palladium catalyst: Support effect. *Appl. Catal. A*1996;134(2):203-215.

15. Zheng Q, Zhou S, Lail M, Amato K. Oxygen removal from oxy-combustion flue gas for CO_2 purification via catalytic methane oxidation. *Ind. Eng. Chem. Res.* 2018;57(6):1954-1960.

16. Kuhn AN, Chen Z, Lu Y, Yang H. Sequential oxygen reduction and adsorption for carbon dioxide purification for flue gas applications.*Energy Technol.* 2019;7(4):1800917.

17. Cullis CF, Willatt BM. Oxidation of methane over supported precious metal catalysts. *J. Catal.* 1983;83(2):267-285.

18. Fujimoto K, Ribeiro FH, Avalos-Borja M, Iglesia E. Structure and reactivity of PdO_x/ZrO_2 catalysts for methane oxidation at low temperatures. *J. Catal.*1998;179(2):431-442.

19. Schmal M, Souza MMVM, Alegre VV, da Silva MAP, César DV, Perez CAC. Methane oxidation - effect of support, precursor and pretreatment conditions - in situ reaction XPS and DRIFT. *Catal. Today.*2006;118(3-4):392-401.

20. Weng X, Ren H, Chen M, Wan H. Effect of surface oxygen on the activation of methane on palladium and platinum surfaces. *ACS Catal.* 2014;4:2598-2604.

21. Singh J, Nachtegaal M, Alayon EMC, Stötzel J, van Bokhoven JA. Dynamic structure changes of a heterogeneous catalyst within a reactor: Oscillations in CO Oxidation over a supported platinum catalyst.*ChemCatChem* 2010;2(6):653-657.

22. Makeev AG, Slinko MM, Luss D. Mathematical modeling of oscillating CO oxidation on Pt-group metals at near atmospheric pressure: Activity of metallic and oxidized surfaces. *Appl. Catal. A*2019;571:127-136.

23. Yang S, Maroto-Valiente A, Benito-Gonzalez M, Rodriguez-Ramos I, Guerrero-Ruiz A. Methane combustion over supported palladium catalysts I. Reactivity and active phase. *Appl. Catal. B*2000;28(3-4):223-233.

24. Ortloff F, Bohnau J, Graf F, Kolb T. Removal of oxygen from (bio-)methane via catalytic oxidation of CH_4-Reaction kinetics for very low O_2:CH_4 ratios.*Appl. Catal. B* 2016;182:375-384.

25. Wang ZM, Yang G, Biswas P, Bresser W, Boolchand P. Processing of iron-doped titania powders in flame aerosol reactors. *Powder Technol.* 2001;114(1-3):197-204.

26. Tiwari V, Jiang J, Sethi V, Biswas P. One-step synthesis of noble metal-titanium dioxide nanocomposites in a flame aerosol reactor.*Appl. Catal. A* 2008;345(2):241-246.

27. Dhumal SY, Daulton TL, Jiang J, Khomami B, Biswas P. Synthesis of visible light-active nanostructured TiO_x ($x < 2$) photocatalysts in a flame aerosol reactor. *Appl. Catal. B*2009;86(3-4):145-151.

28. Strobel R, Pratsinis SE. Flame aerosol synthesis of smart nanostructured materials. *J. Mater. Chem.* 2007;17(45):4743-4756.

29. Niu F, Li S, Zong Y, Yao Q. Catalytic behavior of fame-made Pd/TiO_2 nanoparticles in methane oxidation at low temperatures. *J. Phys. Chem. C.* 2014;118(33):19165-19171.

30. Stark WJ, Wegner K, Pratsinis SE, Baiker A. Flame aerosol synthesis of vanadia-titania nanoparticles: Structural and catalytic properties in the selective catalytic reduction of NO by NH_3. *J. Catal.* 2001;197(1):182-191.

31. Strobel R, Pratsinis SE, Baiker A. Flame-made $Pd/La_2O_3/Al_2O_3$nanoparticles: thermal stability and catalytic behavior in methane combustion. *J. Mater. Chem. C* 2005;15(5):605-610.

32. Fujiwara K, Müller U, Pratsinis SE. Pd subnano-clusters on TiO_2 for solar-light removal of NO. *ACS Catal.*2016;6(3):1887-1893.

33. Fujiwara K, Pratsinis SE. Atomically dispersed Pd on nanostructured TiO_2 for NO removal by solar light. *AIChE J.*2017;63(1):139-146.

34. Wang WN, An WJ, Ramalingam B, Mukherjee S, Niedzwiedzki DM, Gangopadhyay S, Biswas P. Size and structure matter: Enhanced CO_2 photoreduction efficiency by size-resolved ultrafine Pt nanoparticles on TiO_2 single crystals. *J. Am. Chem. Soc.* 2012;134(27):11276-11281.

35. Kumfer BM, Shinoda K, Jeyadevan B, Kennedy IM. Gas-phase flame synthesis and properties of magnetic iron oxide nanoparticles with reduced oxidation state. *J. Aerosol Sci.* 2010;41(3):257-265.

36. Willis JJ, Goodman ED, Wu L, Riscoe AR, Martins P, Tassone CJ, Cargnello M. Systematic identification of promoters for methane oxidation catalysts using size- and composition-controlled Pd-based bimetallic nanocrystals. *J. Am. Chem. Soc.*2017;139(34):11989-11997.

37. Li S, Ren Y, Biswas P, Tse SD. Flame aerosol synthesis of nanostructured materials and functional devices: Processing, modeling, and diagnostics. *Prog. Energy Combust. Sci.* 2016;55:1-59.

38. Ghazzal MN, Wojcieszak R, Raj G, Gaigneaux EM. Study of mesoporous CdS-quantum-dot-sensitized TiO_2 films by using X-ray photoelectron spectroscopy and AFM. *Beilstein J. Nanotechnol.*2014;5:68-76.

39. Masiala TM, Bantu AKM, Bakambo GE, Lunguya JM, Kanza JLK, Muamba OM. Influence of pH preparation on the photo-response of electrodeposited titanium dioxide (TiO_2) thin films. *International Journal of Materials Science and Applications.* 2016;5:207-213.

40. Liu P, Chen TP, Li XD, Liu Z, Wong JI, Liu Y, Leong KC. Effect of exposure to ultraviolet-activated oxygen on the electrical characteristics of amorphous indium gallium zinc oxide thin film transistors. *Ecs Solid State Lett.* 2013;2(4):Q21-Q24.

41. Kannisto H, Arve K, Pingel T, Hellman A, Härelind H, Eränen K, Olsson E, Skoglundh M, Murzin DY. Murzin, On the performance of Ag/Al_2O_3 as a HC-SCR catalyst - influence of silver loading, morphology and nature of the reductant. *Catal. Sci. Technol.* 2013;3(3):644-653.

42. Murzin DY. On cluster size dependent activity and selectivity in heterogeneous catalysis. *Catal. Lett.* 2012;142(11):1279-1285.

43. Hellman A, Resta A, Martin NM, Gustafson J, Trinchero A, Carlsson PA, Balmes O, Felici R, van Rijn R, Frenken JWM, Andersen JN, Lundgren E, Grönbeck H. The active phase of palladium during methane oxidation. *J. Phys. Chem. Lett.* 2012;3(6):678-682.

44. Crampton AS, Rötzer MD, Ridge CJ, Yoon B, Schweinberger FF, Landman U, Heiz U. Assessing the concept of structure sensitivity or insensitivity for sub-nanometer catalyst materials. *Surf. Sci.*2016;652:7-19.

45. Benson JE, Kohn HW, Boudart M. On the reduction of tungsten trioxide accelerated by platinum and water. *J. Catal.* 1966;5(2):307-&.

46. Ostrovskii V. Surface "Homogeneity vs. Heterogeneity" problem for thermally stabilized crystalline bodies and the nature of heterogeneous catalysis. *Journal "Scientific Isrel- Technological Advantages".*2011;13(4).

47. Bissette AJ, Fletcher SP. Mechanisms of autocatalysis. *Angew. Chem. Int. Ed.* 2013;52(49):12800-12826.

48. Masunov AE, Wait E, Vasu SS. Chemical reaction $CO+OH^*$-CO_2+H^*autocatalyzed by carbon dioxide: Quantum chemical study of the potential energy surfaces. *J. Phys. Chem. A* 2016;120(30):6023-6028.

49. Yang Y, Mims CA, Mei DH, Peden CHF, Campbell CT. Mechanistic studies of methanol synthesis over Cu from $CO/CO_2/H_2/H_2O$ mixtures: The source of C in methanol and the role of water. *J. Catal.*2013;298:10-17.

Table 1. Total Pd loading, total Pd mass in 10 mg of Pd-TiO_2 catalyst ($M_{\text{Total Pd}}$), and the average size of Pd-TiO_2 particle ($d_{av,\ Pd-TiO_2}$), and the average size of Pd subnano-cluster/nanoparticle ($d_{av,\ Pd}$) as determined from ICP-MS, FESEM-EDS and STEM analyses.

	Pd precursor feed concentration (mM)	Total Pd loading[a] (wt%)	Total Pd loading[b] (wt%)	$M_{\text{Total Pd}}$ (μg)	$d_{av,\ Pd-TiO_2}$ (nm)[c]	$d_{av,\ Pd}$ (nm)[c]
catalyst 1	0.5	0.24	0.21	23.98	7.57 ± 2.19	<0.5
catalyst 2	1.0	0.45	0.44	45.30	7.18 ± 2.07	0.51 ± 0.12
catalyst 3	1.3	0.76	0.75	75.96	7.61 ± 2.11	0.66 ± 0.16
catalyst 4	2.1	1.08	1.00	107.91	7.14 ± 1.04	0.85 ± 0.17
catalyst 5	3.0	1.25	1.25	125.25	7.34 ± 1.91	1.04 ± 0.18

	Pd precursor feed concentration (mM)	Total Pd loading[a] (wt%)	Total Pd loading[b] (wt%)	$M_{\text{Total Pd}}$ (μg)	$d_{av,\ Pd-TiO_2}$ (nm)[c]	$d_{av,\ Pd}$ (nm)[c]
[a] Total Pd loading was determined by ICP-MS. [b] Total Pd loading was determined by FESEM-EDS. [c] Sizes were determined by STEM (see Figure 2).	[a] Total Pd loading was determined by ICP-MS. [b] Total Pd loading was determined by FESEM-EDS. [c] Sizes were determined by STEM (see Figure 2).	[a] Total Pd loading was determined by ICP-MS. [b] Total Pd loading was determined by FESEM-EDS. [c] Sizes were determined by STEM (see Figure 2).	[a] Total Pd loading was determined by ICP-MS. [b] Total Pd loading was determined by FESEM-EDS. [c] Sizes were determined by STEM (see Figure 2).	[a] Total Pd loading was determined by ICP-MS. [b] Total Pd loading was determined by FESEM-EDS. [c] Sizes were determined by STEM (see Figure 2).	[a] Total Pd loading was determined by ICP-MS. [b] Total Pd loading was determined by FESEM-EDS. [c] Sizes were determined by STEM (see Figure 2).	[a] Total Pd loading was determined by ICP-MS. [b] Total Pd loading was determined by FESEM-EDS. [c] Sizes were determined by STEM (see Figure 2).

Table 2. Fractions of metallic Pd, PdO and intermediate PdO_x as determined from XPS analysis, masses of metallic Pd ($M_{\text{metallic Pd}}$), PdO (M_{PdO}) and intermediate PdO_x (M_{PdO_x}), and total surface area of metallic Pd ($\text{TSA}_{\text{metallic Pd}}$), PdO ($\text{TSA}_{\text{PdO}}$) and intermediate PdO_x($\text{TSA}_{\text{PdO}_x}$).

catalyst 1
catalyst 2
catalyst 3
catalyst 4
catalyst 5

[a] The molecular weight of PdO_x was assumed to be the average of the molecular weights of the metallic Pd and PdO. [b] Th

Table 3. O_2 and CH_4 conversion, and apparent reaction rate constant (k_{app}) with TiO_2, catalyst 1, catalyst 2, catalyst 3, catalyst 4 and catalyst 5 at 723 K.

	O_2 conversion (%)	CH_4 conversion (%)	k_{app} (min^{-1})
TiO_2	30.9	50.7	7.71
catalyst 1	55.8	64.4	17.01
catalyst 2	67.0	81.9	23.10
catalyst 3	77.0	92.4	30.62
catalyst 4	75.3	93.8	29.13
catalyst 5	70.1	93.0	25.15

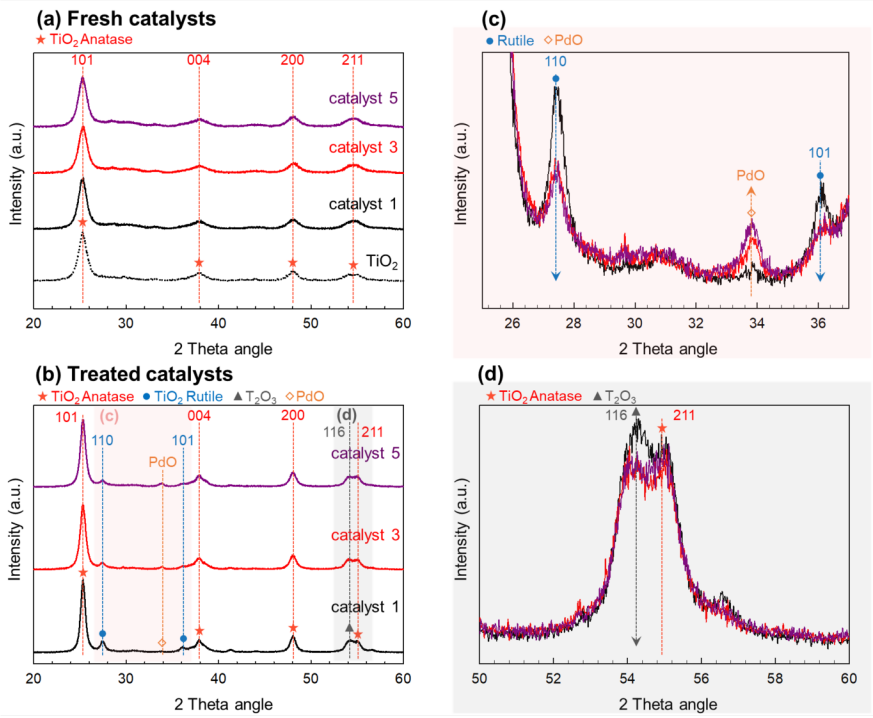

Figure 1. XRD patterns of a) fresh catalysts and b-d) treated catalysts.

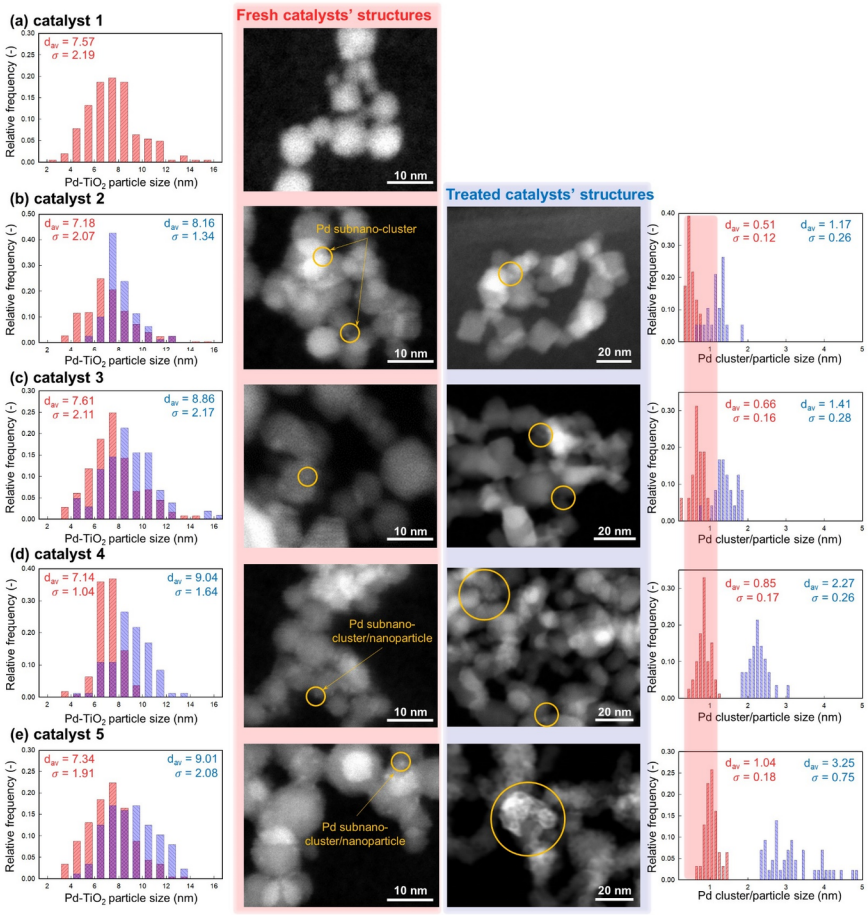

Figure 2. Bulk Pd-TiO_2 nano particle and Pd subnano cluster/nano particle size distributions, and STEM images of a) catalyst 1, b) catalyst 2, c) catalyst 3, d) catalyst 4, and e) catalyst 5. Results related to the fresh catalysts are denoted with red-color and results related to the treated catalysts are shown with blue-color.

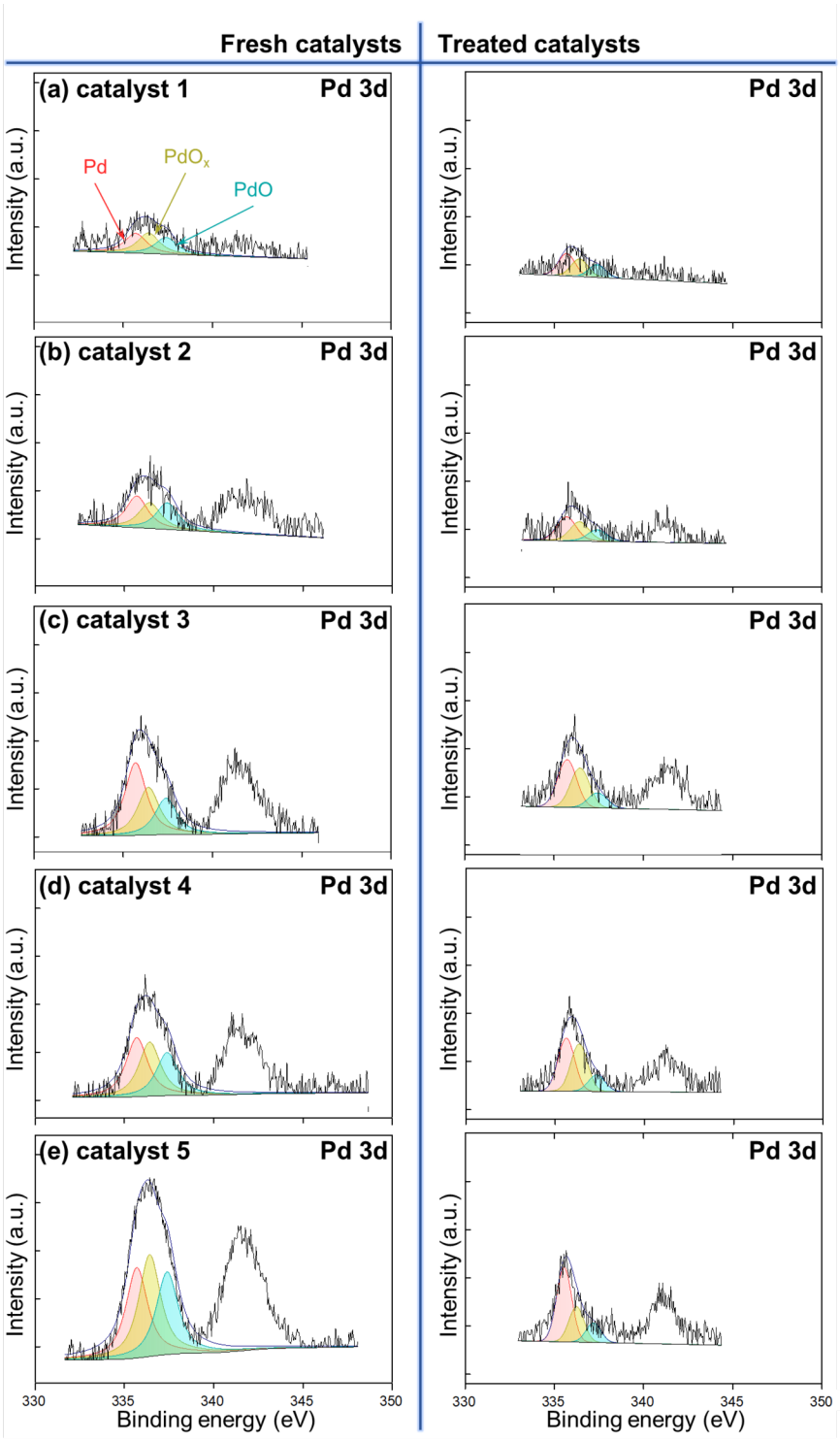

Figure 3. XPS spectra of fresh and treated Pd-TiO_2catalysts: Pd metal (black, 335.7 eV), PdO_x (dark gray, 336.42 eV), PdO (gray, 337.4 eV).

Hosted file

image4.emf available at https://authorea.com/users/308763/articles/440166-flame-synthesis-of-pd-tio2-nanocomposite-catalyst-for-oxygen-removal-from-co2-rich-streams-in-oxy-combustion-exhaust

Hosted file

image5.emf available at https://authorea.com/users/308763/articles/440166-flame-synthesis-of-pd-tio2-nanocomposite-catalyst-for-oxygen-removal-from-co2-rich-streams-in-oxy-combustion-exhaust

Figure 5. (a) Variation of the apparent reaction rate constant (k_{app}) with (a) Pd loading, (b) the fraction of the total surface area of metallic Pd in the fresh catalysts (α_{fresh}), (c) the fraction of the total surface area of metallic Pd in the treated catalysts ($\alpha_{treated}$), and (d) the average fraction of the total surface area of metallic Pd (α_{avg}) at different temperatures.

Hosted file

image6.emf available at https://authorea.com/users/308763/articles/440166-flame-synthesis-of-pd-tio2-nanocomposite-catalyst-for-oxygen-removal-from-co2-rich-streams-in-oxy-combustion-exhaust

Figure 6. (a) O_2 and (b) CH_4 conversion vs. temperature with catalyst 3 under different initial compositions (0%, 53%, and 95% of CO_2 in balance He).

Hosted file

image7.emf available at https://authorea.com/users/308763/articles/440166-flame-synthesis-of-pd-tio2-nanocomposite-catalyst-for-oxygen-removal-from-co2-rich-streams-in-oxy-combustion-exhaust

Hosted file

image8.emf available at https://authorea.com/users/308763/articles/440166-flame-synthesis-of-pd-tio2-nanocomposite-catalyst-for-oxygen-removal-from-co2-rich-streams-in-oxy-combustion-exhaust